X-ray phase-contrast CO_2 angiography for sub-10 μm vessel imaging

2012 Phys. Med. Biol. 57 7431

(http://iopscience.iop.org/0031-9155/57/22/7431)

IOP PUBLISHING PHYSICS IN MEDICINE AND BIOLOGY

Phys. Med. Biol. **57** (2012) 7431–7441 doi:10.1088/0031-9155/57/22/7431

X-ray phase-contrast CO_2 angiography for sub-10 μm vessel imaging

U Lundström[1], D H Larsson[1], A Burvall[1], L Scott[2], U K Westermark[3], M Wilhelm[3], M Arsenian Henriksson[3] and H M Hertz[1]

[1] Biomedical and X-Ray Physics, Department of Applied Physics, KTH Royal Institute of Technology/Albanova, 10691 Stockholm, Sweden
[2] Department of Women's and Children's Health, Karolinska Institutet, 17176 Stockholm, Sweden
[3] Department of Microbiology, Tumor and Cell Biology (MTC), Karolinska Institutet, 17165 Stockholm, Sweden

E-mail: ulf.lundstrom@biox.kth.se

Received 1 August 2012, in final form 17 September 2012
Published 24 October 2012
Online at stacks.iop.org/PMB/57/7431

Abstract

X-ray in-line phase contrast has recently been combined with CO_2 angiography for high-resolution small-animal vascular imaging at low radiation dose. In this paper we further investigate the potential and limitations of this method and demonstrate observation of vessels down to 8 μm in diameter, considerably smaller than the 60 μm previously reported. Our in-line phase-contrast imaging system is based on a liquid-metal-jet-anode x-ray source and utilizes free-space propagation to convert phase shifts, caused by refractive index variations, into intensity differences. Enhanced refractive index variations are obtained through injection of CO_2 gas into the vascular system to replace the blood. We show rat-kidney images with blood vessels down to 27 μm in diameter and mouse-ear images with vessels down to 8 μm. The minimum size of observable blood vessels is found to be limited by the penetration of gas into the vascular system and the signal-to-noise ratio, i.e. the allowed dose. The diameters of vessels being gas-filled depend on the gas pressure and follow a simple model based on surface tension. A theoretical signal-to-noise comparison shows that this method requires 1000 times less radiation dose than conventional iodine-based absorption contrast for observing sub-50 μm vessels.

(Some figures may appear in colour only in the online journal)

1. Introduction

Imaging of blood vessels is crucial to develop our understanding of angiogenesis (McDonald and Choyke 2003) and in the assessment of angiogenesis inhibitors used in, e.g., cancer treatment (Folkman 2006). We have previously shown that x-ray in-line phase contrast can be combined with CO_2 angiography to image vessels with diameters down to 60 μm at a

dose acceptable for living animals (Lundström *et al* 2012). In this paper we demonstrate such low-dose imaging of microvasculature down to 8 μm, well beyond current x-ray methods, and investigate the limitations of the method for detection of very small blood vessels.

Present methods for imaging blood vessels divide into two major groups. The first is clinical methods such as computed tomography (CT), magnetic resonance imaging (MRI), positron emission tomography (PET) and ultrasonography, and their higher-resolution counterparts for small animal imaging (Kagadis *et al* 2010, Badea *et al* 2008). These methods can all be used to image thick objects, but are unable to resolve the microvasculature. Micro-CT has the highest resolution of these methods but can still only observe vessels down to 50 μm in diameter (Lundström *et al* 2012). The second group is optical methods such as confocal microscopy, multiphoton microscopy (MPM) (Maurin *et al* 2011) and optical frequency domain imaging (OFDI) (Vakoc *et al* 2009). These have high resolution but work well only in the first few hundred μm of tissue (McDonald and Choyke 2003). Presently no non-destructive method allows visualization of the microvasculature of a full mouse *in vivo* or even a few millimeters thick tissue *in vitro*.

X-ray phase-contrast imaging has been investigated for a wide range of biomedical applications demonstrating, e.g., increased soft-tissue discrimination and reduced dose (Lewis 2004, Fitzgerald 2000). The method relies on differences in the refractive index within the studied object which result in variations in the phase of the wavefront emerging from the object. This can be measured in several ways, e.g., in differential phase contrast using a grating system (Momose 2005, Pfeiffer *et al* 2006) or, as is done here, with in-line phase contrast (Wilkins *et al* 1996) where the wavefront is allowed to propagate and turn phase variations into intensity variations. In-line phase contrast requires no optics, only the source, object and detector, making the arrangement simple. X-ray phase contrast has previously been used to image blood vessels (Laperle *et al* 2008, Momose *et al* 2000). However, at best, observation of vessels down to 20 μm has been demonstrated and then at dose levels incompatible with living tissue.

Lundström *et al* (2012) introduced the idea of using CO_2 gas as a contrast agent for phase-contrast imaging to allow observation of small blood vessels. The method was demonstrated by imaging of the venous system of a rat kidney, producing tomographic images showing vessels down to 60 μm in diameter. The required radiation dose is small compared to absorption micro-CT and previous phase-contrast methods, granting the possibility of performing longitudinal studies. We note that CO_2 is already used clinically as an x-ray contrast agent by injecting it into the blood stream to temporarily replace the blood and thereby reduce the x-ray absorption in the vessels (Cho and Hawkins 2007).

In this paper, we show that phase-contrast CO_2 microangiography can be used to observe 27 μm diameter vessels in a rat kidney as well as sub-10 μm vessels in a mouse ear. Both experiments were performed at dose levels acceptable for studies on living animals (Badea *et al* 2008). Furthermore, we investigate the limits of the method and conclude that the smallest observable size of vessels is presently limited by surface tension that prohibits the filling of the vessels with gas, and by the photon noise, i.e. dose. To our knowledge we demonstrate the highest-resolution x-ray microangiography to date. The method has the potential to fill the gap between the clinical and optical methods discussed above, thereby opening up for studies of, e.g., early blood vessel formation.

2. Materials and methods

Figure 1 shows the experimental arrangement. X-ray in-line phase-contrast imaging requires only an x-ray source, an object and an x-ray detector, but places high demands on the source

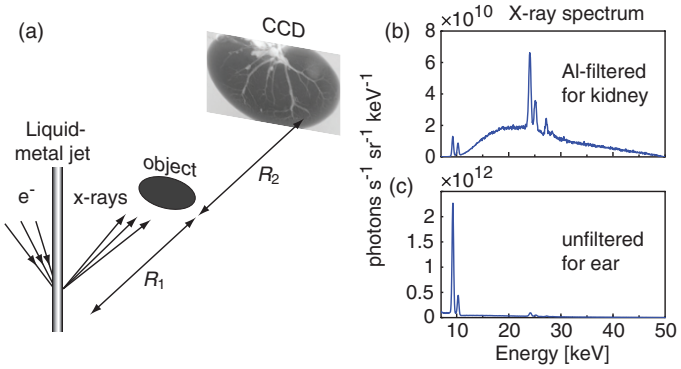

Figure 1. The x-ray in-line phase-contrast system (a) consists only of the x-ray source, the object and the detector. The emission spectrum of the liquid-metal-jet-anode x-ray source filtered with 0.5 mm thick aluminum (b) and unfiltered (c).

size and detector resolution. The x-ray source used here is a liquid-metal-jet-anode electron-impact x-ray source (Hemberg *et al* 2003) similar to the one described by Larsson *et al* (2011) but with Galinstan (Ga/In/Sn alloy) as jet material. An electron beam of 0.8 mA current and 50 kVp acceleration voltage was focused onto the metal jet at 45° angle between surface normal and electron beam as well as between surface normal and x-ray output. The source size was measured with zone-plate imaging to be circular, almost Gaussian, and to have a full width at half maximum (FWHM) of 10 μm for the rat-kidney experiment and 7 μm for the mouse-ear experiments. For the kidney experiment the low-energy part of the spectrum was filtered away using 0.5 mm of aluminum to reduce the radiation dose, giving the spectrum in figure 1(b). For the ear experiments the unfiltered spectrum of figure 1(c) was used. All doses were calculated from the absorbed energy using mass energy–absorption coefficients from NIST (Hubbell and Seltzer 2011) and measured x-ray spectra.

The images were acquired using a Photonic Science VHR x-ray camera with a 5 mg cm^{-2} Gadox scintillator coupled fiber optically 1:1 to a 2.4×3.6 cm^2 CCD with 9 μm pixels.

The imaging system was simulated using a Fourier-based wave-propagation method as described by Lundström *et al* (2012). The simulation system takes into account the spectrum and intensity distribution of the source, the detector modulation transfer function, noise power spectrum (NPS), energy-dependent absorption efficiency and readout noise, as well as absorption in air and object holder. Because of the thin objects, long distances, and relatively small detector area, few Compton-scattered photons will reach the detector. The scattered-to-primary ratio is in the order of 5×10^{-6} for both the kidney and ear-imaging presented here. Compton-scattered photons are therefore treated as absorbed in the simulations.

We have imaged two kinds of biological samples[4]. The first is a freshly excised rat kidney. During imaging the $7 \times 21 \times 13$ mm^3 kidney was immersed in nutrient solution and held in place between two 0.5 mm thick PMMA sheets. The kidney was gently injected with CO_2 through a plastic tube inserted into the main renal artery using a syringe pump, allowing the pressure to reach a maximum of 95 mbar, well below the normal blood pressure of rats (Mattson 2001).

The second type of sample is mouse ear, with and without hair. Here the venal system was injected with CO_2 or air through a 36 gauge syringe needle (110 μm outer diameter). The

[4] All animal experiments were performed according to the Karolinska Institutet regulations concerning care and use of laboratory animals, and were approved by the Stockholm North ethical evaluation board for animal research.

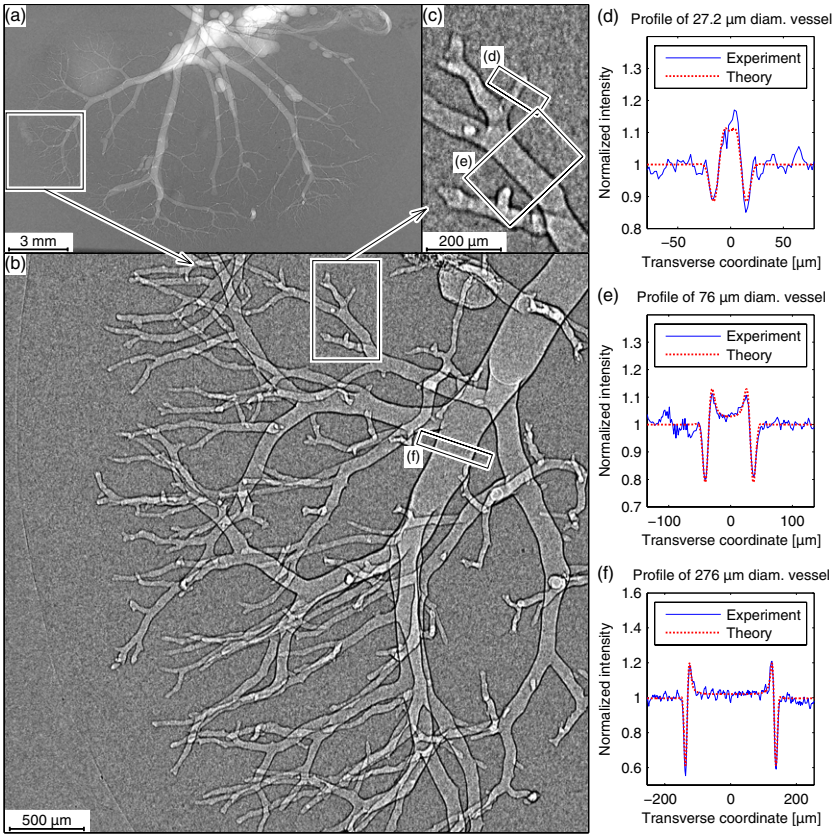

Figure 2. 120 mGy images of a rat kidney with its arterial system filled with CO_2 gas. (a) An overview of the whole kidney taken with $R_1 = 0.6$ m and $R_2 = 0.4$ m. (b) The area of the kidney indicated in (a) imaged with $R_1 = 1.2$ m and $R_2 = 4.8$ m to lower the dose and increase contrast. (c) A zoom-in on the indicated part in (b). (d)–(f) Profiles of vessels of varying diameter compared to our simulations of same-width vessels. The areas used to calculate the graphs are marked in (b) and (c). The contrast varies between vessels and is typically 70–105% of the contrast in the simulations. The exposure times were 185 s (a), and 1000 s (b)–(c).

pressure was in this case increased step-wise up to 220 mbar which was the highest pressure the vessels held for.

3. Results

Figure 2 shows images of the arterial system of a rat kidney. Figure 2(a) is a low-magnification ($M = 1.7$) overview image of the full kidney obtained with source-to-object distance $R_1 = 0.6$ m and object-to-detector distance $R_2 = 0.4$ m. To see the smaller vessels more clearly, a higher-magnification ($M = 5$) image with longer distances ($R_1 = 1.2$ m and $R_2 = 4.8$ m) is shown in figures 2(b) and (c). The characteristic edge enhancement of in-line phase contrast carries almost all the information in these images. The dose was 120 mGy and the exposure time ranged from 185 to 1000 s.

To measure the widths of the vessels we integrate the pixel values along straight sections of the vessels to obtain the cross-sectional profiles with relatively low noise. The profiles are

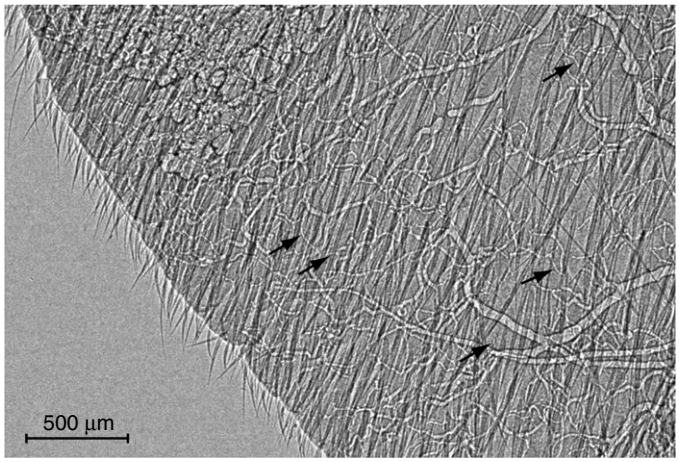

Figure 3. X-ray in-line phase-contrast image of a (hairy) mouse ear. The venal system is injected with CO_2 gas to give it high contrast. Arrows point at some of the smallest vessels, with diameters between 9 and 11 μm. The source-to-object distance is $R_1 = 0.6$ m and the object-to-detector distance is $R_2 = 2.4$ m. Evacuated tubes are inserted in the beam path to avoid absorption of the 9.25 keV x-rays. Exposure time is 10 s giving 30 mGy radiation dose.

compared to simulated profiles in a range of diameters with 100 nm increments. For each simulated diameter different relative translations of the profiles are tested to find the minimum root-mean-square error. The vessel diameter giving the least such error is considered to be the diameter of the vessel. Figures 2(d)–(f) demonstrate good agreement between images and simulations for vessels of all diameters found in the kidney, from the smallest 27 μm vessels to the largest 280 μm vessel.

Figure 3 shows CO_2 microangiography of a mouse ear. The blood vessels were injected with 220 mbar of carbon dioxide gas. With this arrangement the dose was 30 mGy and the exposure time 10 s. We observe vessels down to below 9 μm in diameter. It is, however, obvious that the hair with its strong phase contrast is a complication, producing a background pattern that makes the observation of the blood vessels less clear. Similar images of a nude-mouse ear are shown in figure 4.

The mouse ear is only 200 μm thick which allows us to use the strong 9.25 keV Ga K_α emission line of our galinstan liquid-metal-jet-anode x-ray source. This reduces the exposure time considerably compared to the kidney images in figure 2 for three reasons. First, there are about five times more photons in the 9.25 keV emission line compared to the total number of photons between 15 and 25 keV that was used for the kidney images. Second, the difference in the real part of the refractive index is 4.6 times higher at 9.25 keV compared to 20 keV, which gives 4.6 times higher contrast for the small vessels. Third, the detection efficiency of our 5 mg cm^{-2} Gadox scintillator is only 17% at 20 keV, instead of 75% at 9.25 keV, which shortens the exposure time by an additional factor of 4.4. A disadvantage of this low-energy radiation is that the attenuation length in tissue is about 1.5 mm, so that objects thicker than a few mm cannot be imaged successfully.

The short attenuation length also makes air absorption a problem when long propagation distances are used. For this reason the experiment of figure 3 which uses relatively long distances ($R_1 = 0.6$ m and $R_2 = 2.4$ m) requires evacuated tubes inserted in the beam path. We use standard KF50 tubes with 25 μm thick Kapton films clamped to the ends. The evacuated

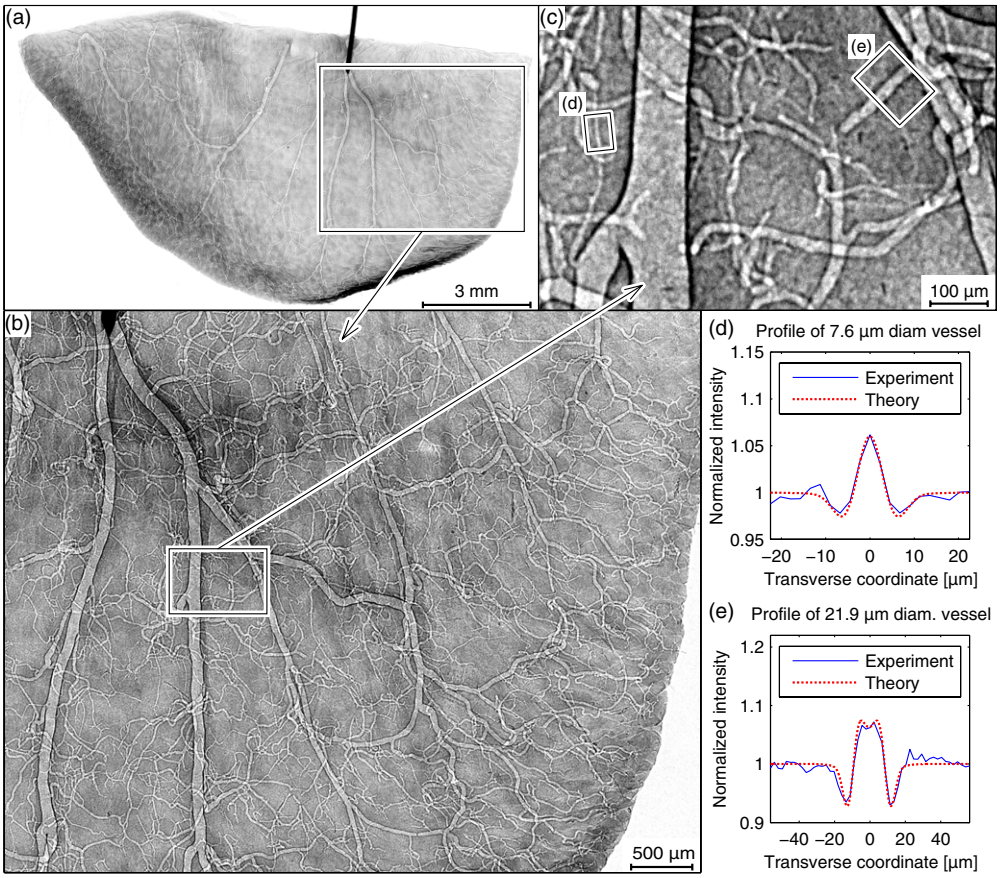

Figure 4. Images of a nude-mouse ear with its venous system filled with gas. (a) An overview showing the cut-off ear and the needle used to inject air, imaged with $R_1 = R_2 = 0.15$ m. (b) The indicated part of (a) imaged with $R_1 = 0.15$ m and $R_2 = 0.45$ m. The dose was 500 mGy and the exposure time 10 s. (c) A zoom-in on the indicated part in (b). (d)–(e) Vessel profiles from the marked areas in (c) compared to simulated profiles of the same widths.

length was 0.35 m between source and object and 2.3 m between object and detector. The experiment of figure 4 instead uses considerably shorter distances.

Figure 4 shows the venous system of a nude-mouse ear. For simplicity, air was used instead of CO_2 in these recordings. Furthermore, the distances were much shorter than in figure 3, thereby avoiding the additional complication of the vacuum tubes. Figure 4(a) gives a low-magnification overview of the cut-off ear and the needle used to inject air. The gas pressure was 220 mbar for these images. In the higher-magnification images of figures 4(b) and (c) even the smallest filled vessels of ∼8 µm diameter are clearly visible. The exposure time was 10 s and the radiation dose was 500 mGy, considerably higher than for figure 3 because of the shorter distances.

Figures 3 and 4 shows that vessels below 10 µm can be both gas-filled and imaged using in-line phase contrast at reasonable doses and exposure times. Figures 4(d) and (e) show vessel intensity profiles obtained in the same way as those in figure 2. They demonstrate good agreement between experiment and simulations also for these imaging parameters and

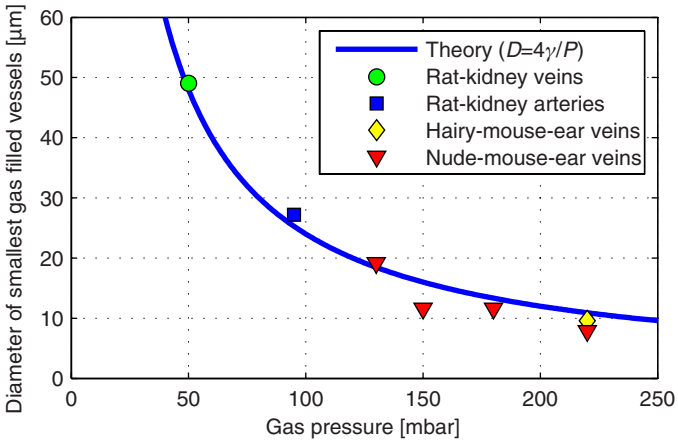

Figure 5. A plot of the diameter of the smallest blood vessels that will be gas-filled as function of the gas pressure. The line corresponds to force equilibrium for the surface tension of blood at 21 °C, $\gamma = 60$ mN m^{-1}. The marks corresponds to the pressures and smallest vessels found in Lundström *et al* (2012) (green circle), figure 2 (blue square), figure 3 (yellow diamonds) and figure 4 (red triangles).

for vessels down to 8 μm in diameter. Simulations show that with the imaging parameters of figure 4(b) the width measurement of vessels with 8 μm diameter has a standard error of 0.7 μm. This simulation does not take into account anatomical noise, but photon noise, which is the larger noise source at this dose level. The corresponding error for 20 μm diameter vessels is 0.2 μm. An image of the same ear as in figure 4, but with longer exposure time indicates vessel diameters of 7.9 μm and 22.1 μm instead of the 7.6 μm and 21.9 μm shown in figures 4(d) and (e), both within the error margin.

4. Discussion

The minimum observable blood vessel size is fundamentally limited by source size and detector resolution, but practically limited by photon noise and, thus, by the dose. This limitation is discussed in more detail below. However, the method is also limited by the surface tension of blood, since it prevents gas from reaching the smallest vessels. The theoretically smallest diameter of vessels to be filled with gas can be calculated from the gas pressure. When the contact angle is close to zero, as in our case, the relationship is (Lundström *et al* 2012)

$$D = \frac{4\gamma}{P}, \tag{1}$$

where D is the vessel diameter, P is the pressure and γ is the blood surface tension. Equation (1) is plotted in figure 5 for a surface tension of $\gamma = 60$ mN m^{-1}, the surface tension of human blood at 21 °C (Rosina *et al* 2007). In figure 5 we have also included experimentally determined minimum vessel diameter at different pressures. These data points are from the kidney image of figure 2 (blue square), the ear image of figure 3 (yellow diamond), the ear image of figure 4 and images of the same ear as in figure 4 but at earlier times and lower pressures (red triangles), and the kidney venous system of Lundström *et al* (2012) (green circle). For all images the minimum vessel diameter is taken as the average diameter over the five smallest vessels we found, to prevent individual vessels from having a too large effect. The images were manually scanned for small vessels, which were marked and measured automatically

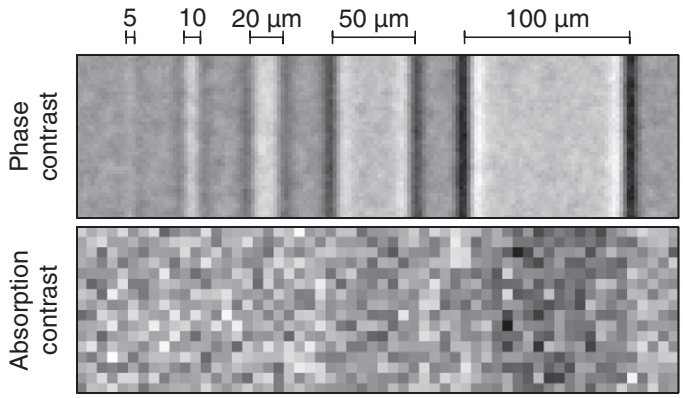

Figure 6. Simulated images of blood vessels ranging from 5 µm to 100 µm in diameter in phase and absorption contrast. The upper part is simulated using the imaging parameters of figure 4(b). The vessels are gas-filled in 200 µm thick tissue. The gray scale goes from 0.82 (black) to 1.12 (white) in normalized units. The lower part is simulated as an ideal absorption-contrast system for vessels with a CT-number of 1000 HU. Both parts have an exposure of 500 mGy. The pixel size is increased in the absorption-contrast simulation to make it easier to see the larger vessels. The gray scale in the lower part goes from 0.993 (black) to 1.005 (white) in normalized units. This illustrates the improved image quality of phase-contrast imaging over absorption imaging for small vessels.

in the way described earlier. We conclude that the experiments follow our theoretical model closely. Thus, it is possible to predict the minimum diameter of the vessels which are filled with gas provided the pressure is in the non-damaging range used here.

Figure 6 illustrates the improved visibility of vessels using our phase-contrast system compared to an ideal absorption-contrast system. The upper part of figure 6 is simulated with all parameters equal to those used in the mouse-ear imaging of figure 4(b). The vessels are gas-filled cylinders in 200 µm thick tissue. The exposure time is 10 s, giving a radiation dose of 500 mGy. The simulation takes into account air and object absorption, the source intensity distribution and spectrum, and the detector modulation transfer function, absorption efficiency and NPS. Note, though, that structural noise (or background) such as that from the hair of figure 3 is not included.

The lower part of figure 6 is simulated for an ideal absorption-contrast system, also with an exposure of 500 mGy. The vessels contain 9.2 mg iodine per ml blood, giving a CT-number of 1000 HU for the monochromatic 35 keV x-rays used in these calculations. The pixels are larger (5 µm in the object plane) than in the phase-contrast case to make it easier to see the low spatial frequencies. For this absorption system, which has a point source and a perfect detector modulation transfer function, the source-to-object and object-to-detector distances have a negligible effect on image quality. With the absorption system the 50 µm vessel can barely be detected, while the phase-contrast system even visualizes the 5 µm vessel when it is this long (100 µm) and straight.

To give quantitative information on what can be detected in an image we use the ideal-observer signal-to-noise ratio (SNR). Following the analysis of Lundström *et al* (2012), we calculate the SNR using equation (13.236) in Barrett and Myers (2004),

$$\mathrm{SNR}^2 = \iint \frac{|\Delta G(\mathbf{u})|^2}{W(\mathbf{u})}\,\mathrm{d}^2u, \tag{2}$$

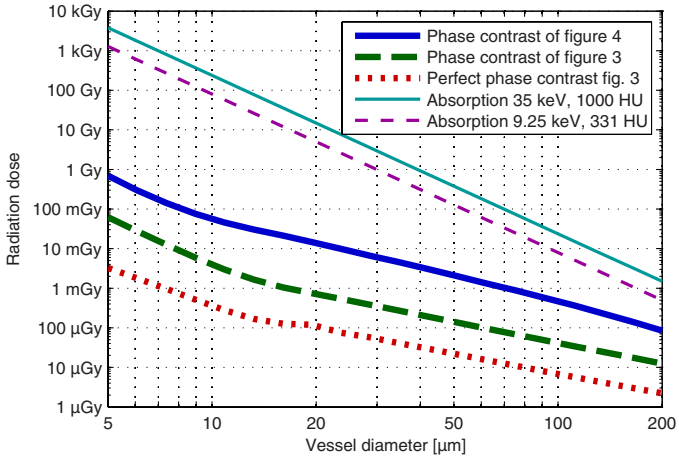

Figure 7. A plot of the dose required to detect blood vessels in a 200 μm thick mouse ear as function of their diameter, using our phase-contrast arrangements (solid blue and dashed green lines), a perfect phase-contrast arrangement with 9.25 keV x-rays (dotted red line), and using absorption contrast with an iodinated contrast agent (thin solid and dashed lines). Absorption imaging is normally done at 35 keV, just above the iodine absorption edge, but requires slightly lower dose at 9.25 keV for this thin sample. Both absorption cases are for 9.2 mg I ml^{-1} blood, which gives CT-numbers of 1000 and 331 HU at 35 and 9.25 keV, respectively. For 10 μm vessels phase contrast requires about 3 to 4 orders of magnitude lower dose than absorption contrast.

where **u** is spatial frequency, ΔG is the Fourier transform of the difference in expected images with and without an object, and W is the NPS. The detectability limit is set to $\mathrm{SNR}^2 = 25$ for a length of the vessel equal to its width.

By simulating images of vessels as in figure 6 and using the detectability criterion explained above we can calculate and plot the dose required to detect vessels as function of their diameter. This is done in figure 7 for five different systems. The first two are our phase-contrast ear-imaging arrangement used for figures 4 and 3. The first one uses $R_1 = 0.15$ m and $R_2 = 0.45$ m and the second $R_1 = 0.6$ m and $R_2 = 2.4$ m and both use gas-filled vessels. The third is an ideal phase-contrast system using monochromatic 9.25 keV radiation and the same imaging distances as in figure 3. It differs from the previous line only in that it has a monochromatic point source and a perfect infinite-resolution detector while the other has all source and detector parameters from our arrangement. The last two systems are ideal absorption-contrast imaging systems using 35 and 9.25 keV x-rays, respectively. Thus, both the source and detector are simulated as perfect. The vessels are filled with iodine with a concentration of 9.2 mg I ml^{-1} blood, corresponding to a CT-number of 1000 HU for 35 keV x-rays. For all lines in figure 7 the tissue thickness is 200 μm, corresponding to the mouse-ear thickness of figures 3 and 4.

Figure 7 shows that in absorption contrast some reduction in required dose can be achieved for objects this thin when using low-energy x-rays instead of staying above the iodine absorption edge. A further reduction in energy would give some additional improvement but limit the method to sub-millimeter-thick objects.

More significantly, figure 7 shows that the CO_2 phase-contrast method allows observation of small-diameter blood vessels at significantly lower dose than with absorption methods. For vessels with diameters on the order of 10 μm the dose is reduced 3 to 4 orders of magnitude compared to any absorption system already with our present phase-contrast arrangement.

Further source and detector development could decrease the dose of phase-contrast imaging another 1 to 2 orders of magnitude with other imaging parameters kept constant. Comparing the lines for figures 3 and 4 we see that the increased propagation distance combined with the evacuated tubes used in figure 3 gives a reduction in dose of about 1 order of magnitude. In figure 7 a dose curve (not shown) corresponding to the kidney imaging of figure 2 follows that for figure 4 imaging conditions (solid blue line), but is about a factor of 10 higher. For analysis on a similar arrangement, see (Lundström *et al* 2012).

5. Conclusions

We have demonstrated that phase-contrast CO_2 microangiography allows imaging of sub-10 μm blood vessels. Measurements were performed at dose levels suitable for studies on living small animals and at gas pressures compatible with the studied vessels. The smallest observable vessel diameter is limited by dose and the maximum allowable gas pressure. Calculations show that the required dose to detect 10 μm vessels is 3 orders of magnitude lower than for x-ray absorption methods, allowing *in vivo* small-animal imaging of the smallest vessels that can be gas-filled.

As mentioned in the introduction there are many methods for vascular imaging, but this is the first that can detect sub-50 μm vessels several mm down into tissue at physiological conditions and at acceptable dose. X-ray micro-CT and digital subtraction angiography are limited to larger vessels because of photon noise and low contrast. Multiphoton microscopy has high resolution, but cannot see further than 600 μm into tissue due to light scattering (Maurin *et al* 2011). Optical frequency domain imaging is a newer method that can detect vessels 2 mm into tissue (Vakoc *et al* 2009), but the image quality at this depth is unclear. Thus, phase-contrast CO_2 microangiography has the potential to fill the gap between the clinical and optical methods in vascular imaging by visualizing smaller vessels than is possible in micro-CT, deeper into tissue than is possible with optical methods.

Exposure times depend on many parameters. We have shown that a 200 μm thick mouse-ear can be imaged in a few seconds. Increasing that thickness to 2 mm would require about three times longer exposure time and twice the dose when using the same 9.25 keV radiation. Thicker objects require higher energy x-rays, which for the present source means longer exposure times. The liquid-metal-jet-anode x-ray source has been proven to work with an indium–tin alloy giving characteristic emission at 25 keV and higher efficiency in the bremstrahlung generation (Larsson *et al* 2011). Elements with even higher atomic numbers might work, but even if no suitable high-Z material can be found, the high loading capacity of the metal jet allows for higher-power bremstrahlung output at higher energies if the acceleration voltage is increased.

The mouse-ear imaging was performed both with a relatively short propagation distance in figure 4 and with longer distances in figure 3. Keeping the magnification constant the contrast is essentially proportional to the effective propagation distance $z = R_1R_2/(R_1+R_2)$. This cancels the reduction in SNR due to the lower photon flux at an increased distance. The required exposure time is therefore almost independent of propagation distance when magnification is kept constant. On the other hand, the radiation dose goes down with the inverse square of the distance. Thus, an increased propagation distance gives a reduced dose for the same image quality and exposure time. The downside is the impracticality of evacuated tubes and relatively higher readout noise.

Finally we note that the imaging method used here is extendible to 3D imaging using tomography (Lundström *et al* 2012) if the images are processed with a phase-retrieval algorithm (e.g., Burvall *et al* 2011) before the 3D reconstruction. This could potentially be done for a whole mouse although it would be computationally demanding and analytical phase-retrieval

algorithms would not be able to reproduce both bones and vessels sharply in the same reconstruction.

Acknowledgments

This work was supported by the Swedish Basic Science Research Council (VR 2009-3142) and the Knut and Alice Wallenberg Foundation (KAW 2011.0136). We thank Per Takman for early contributions and Hjalmar Brismar for discussions.

References

Badea C T, Drangova M, Holdsworth D W and Johnson G A 2008 *In vivo* small-animal imaging using micro-CT and digital subtraction angiography *Phys. Med. Biol.* **53** R319–50

Barrett H H and Myers K J 2004 *Foundations of Image Science* (Hoboken, NJ: Wiley)

Burvall A, Lundström U, Takman P A C, Larsson D H and Hertz H M 2011 Phase retrieval in x-ray phase-contrast imaging suitable for tomography *Opt. Express* **19** 10359–76

Cho K and Hawkins I F 2007 *Carbon Dioxide Angiography* (London: Informa Healthcare)

Fitzgerald R 2000 Phase-sensitive x-ray imaging *Phys. Today* **53** 23–6

Folkman J 2006 Angiogenesis *Annu. Rev. Med.* **57** 1–18

Hemberg O, Otendal M and Hertz H M 2003 Liquid-metal-jet anode electron-impact x-ray source *Appl. Phys. Lett.* **83** 1483–5

Hubbell J H and Seltzer S M 2011 Tables of x-Ray Mass Attenuation Coefficients and Mass Energy-Absorption Coefficients from 1 keV to 20 MeV for Elements Z =1 to 92 and 48 Additional Substances of Dosimetric Interest http://www.nist.gov/pml/data/xraycoef/index.cfm

Kagadis G C, Loudos G, Katsanos K, Langer S G and Nikiforidis G C 2010 *In vivo* small animal imaging: current status and future prospects *Med. Phys.* **37** 6421–42

Laperle C M, Hamilton T J, Wintermeyer P, JWalker E, Shi D X, Anastasio M A, Derdak Z, Wands J R, Diebold G and Rose-Petruck C 2008 Low density contrast agents for x-ray phase contrast imaging: the use of ambient air for x-ray angiography of excised murine liver tissue *Phys. Med. Biol.* **53** 6911–23

Larsson D H, Takman P A C, Lundstrom U, Burvall A and Hertz H M 2011 A 24 keV liquid-metal-jet x-ray source for biomedical applications *Rev. Sci. Instrum.* **82** 123701

Lewis R A 2004 Medical phase contrast x-ray imaging: current status and future prospects *Phys. Med. Biol.* **49** 3573–83

Lundström U, Larsson D H, Burvall A, Takman P A C, Scott L, Brismar H and Hertz H M 2012 X-ray phase contrast for CO_2 microangiography *Phys. Med. Biol.* **57** 2603

Mattson D L 2001 Comparison of arterial blood pressure in different strains of mice *Am. J. Hypertens.* **14** 405–8

Maurin M, Stephan O, Vial J-C, Marder S R and Sanden B v d 2011 Deep *in vivo* two-photon imaging of blood vessels with a new dye encapsulated in pluronic nanomicelles *J. Biomed. Opt.* **16** 036001

McDonald D M and Choyke P L 2003 Imaging of angiogenesis: from microscope to clinic *Nat. Med.* **9** 713–25

Momose A 2005 Recent advances in x-ray phase imaging *Japan J. Appl. Phys.* **44** 6355–67

Momose A, Takeda T and Itai Y 2000 Blood vessels: depiction at phase-contrast x-ray imaging without contrast agents in the mouse and rat—feasibility study *Radiology* **217** 593–6

Pfeiffer F, Weitkamp T, Bunk O and David C 2006 Phase retrieval and differential phase-contrast imaging with low-brilliance x-ray sources *Nature Phys.* **2** 258–61

Rosina J, Kvasnák E, Suta D, Kolárová H, Málek J and Krajci L 2007 Temperature dependence of blood surface tension *Physiol. Res.* **56** S93–8

Vakoc B J *et al* 2009 Three-dimensional microscopy of the tumor microenvironment *in vivo* using optical frequency domain imaging *Nat. Med.* **15** 1219–23

Wilkins S W, Gureyev T E, Gao D, Pogany A and Stevenson A W 1996 Phase-contrast imaging using polychromatic hard x-rays *Nature* **384** 335–8